InSight Bulletin: A Multidisciplinary Interlink International Research Journal
Peer Reviewed International, Open Access Journal.
ISSN : 3065-7857 / Website: https://ibrj.us / Volume-2, Issue-12 / December - 2025

Original Article

Investigation on Iron and Nickel Oxide Nanoparticles Using Combustion Method for Photocatalytic Activity

A. Kesavapriya [1], Venci. X[2], Deepapriya. S[3]
[1,2,3]PG & Research Department of Physics, Auxilium College (Autonomous), Vellore, Tamil Nadu, India.

Manuscript ID:
IBMIIRJ -2025-021227

Submitted: 10 Nov. 2025

Revised: 15 Nov. 2025

Accepted: 20 Dec. 2025

Published: 31 Dec. 2025

ISSN: 3065-7857

Volume-2

Issue-12

Pp. 125-133

December 2025

Correspondence Address:
Deepapriya. S
PG & Research Department of Physics, Auxilium College (Autonomous), Vellore, Tamil Nadu, India.
Email: deepapriyaphysicist@gmail.com

OPEN ACCESS

Quick Response Code:

Web. https://ibrj.us

DOI: 10.5281/zenodo.23362492

DOI Link:
https://doi.org/10.5281/zenodo.23362492

Creative Commons

Abstract

Nanostructured metal oxides have attracted significant attention due to their distinctive physicochemical properties and broad applicability in environmental remediation. In the present study, nickel(II) oxide (NiO) and iron(II) oxide (FeO) nanopowders were synthesized via a combustion method selected for its efficiency and ability to regulate particle size and morphology. The structural, optical, and surface characteristics of the materials were systematically investigated using X-ray diffraction (XRD), UV–Visible spectroscopy, scanning electron microscopy (SEM), transmission electron microscopy (TEM), and Fourier transform infrared (FTIR) spectroscopy. XRD analysis confirmed the formation of crystalline phases with a hexagonal wurtzite structure, exhibiting average crystallite sizes of 12 nm for NiO and 13 nm for FeO. UV–Visible analysis enabled the estimation of optical band gaps through the Kubelka–Munk (K–M) approach, while SEM and TEM provided insights into particle morphology and distribution. FTIR spectra validated the presence of characteristic metal–oxide functional groups. The photocatalytic performance of the synthesized nanoparticles was evaluated for the degradation of water pollutants, demonstrating their potential as effective materials for wastewater purification and other environmental applications.

Keywords: *Metal oxides, Combustion method, Photocatalytic activity.*

Introduction

Nanotechnology has emerged as a rapidly expanding domain owing to the exceptional physicochemical behaviors exhibited by materials at the nanoscale. Among these, transition metal oxides occupy a prominent position in materials research because of their multifunctional applications across sectors such as energy storage, catalysis, ceramics, magnetic devices, and environmental technologies. Nickel(II) oxide (NiO) and iron(II) oxide (FeO), in particular, have been widely investigated due to their stability, tunable electronic properties, and extensive industrial relevance. The growing global demand for clean energy, coupled with increasing concerns over water pollution, has intensified the search for sustainable and effective remediation technologies. Traditional water purification methods often fall short in eliminating persistent organic contaminants, especially those resistant to biological degradation. This challenge has accelerated interest in advanced oxidation processes such as photocatalysis, which employs semiconductor materials activated by light to generate reactive electron–hole pairs capable of mineralizing complex pollutants into benign end products. Conventional semiconductor oxides like NiO and FeO are valued for their abundance, environmental compatibility, and low cost; however, their practical photocatalytic performance is often constrained by intrinsic limitations. These include their relatively wide band gaps, which restrict efficient absorption to the ultraviolet region, and rapid recombination of photogenerated charge carriers, which diminishes catalytic efficiency. To overcome these drawbacks, numerous strategies such as elemental doping, surface functionalization, and the construction of heterostructured composites have been developed to enhance visible-light activity and charge separation dynamics. In recent years, attention has broadened to more complex oxide systems, including perovskite- and spinel-type materials, which offer flexible structural frameworks and adjustable electronic configurations. Tailoring surface properties to achieve high porosity, low density, and large specific surface area has proven essential to improving photocatalytic activity,

Creative Commons (CC BY-NC-SA 4.0)
This is an open access journal, and articles are distributed under the terms of the Creative Commons Attribution-NonCommercial-ShareAlike 4.0 International Public License, which allows others to remix, tweak, and build upon the work noncommercially, as long as appropriate credit is given and the new creations ae licensed under the idential terms.

How to cite this article:
Kesavapriya, A., X, V., & S, D. (2025). Investigation on Iron and Nickel Oxide Nanoparticles Using Combustion Method for Photocatalytic Activity. InSight Bulletin: A Multidisciplinary Interlink International Research Journal, 2(12), 125–133. https://doi.org/10.5281/zenodo.23362492

as these features facilitate greater interaction between pollutants and active catalytic sites.In this study, NiO and FeO nanopowders were synthesized using a combustion-based method selected for its operational simplicity, rapid reaction conditions, and capacity to regulate particle size and morphology. The resulting nanomaterials were subjected to comprehensive characterization to elucidate their structural, optical, and surface features. Structural analysis was carried out using X-ray diffraction (XRD), while surface morphology and particle architecture were examined through transmission electron microscopy (TEM) and scanning electron microscopy (SEM). Fourier transform infrared (FTIR) spectroscopy was employed to identify functional groups and confirm chemical composition. Additionally, UV–Visible spectroscopy was utilized to evaluate optical absorption behavior and estimate band gap energies. The synthesized materials were subsequently assessed for their suitability in photocatalytic applications.

Methodology

Nickel(II) oxide (NiO) and iron(II) oxide (FeO) nanopowders were prepared through the solution combustion synthesis (SCS) method. This technique was chosen in preference to routes utilizing sulfate- or chloride-based precursors, as nitrate-derived reagents decompose to form predominantly gaseous products such as N_2, H_2O, and CO_2, resulting in relatively cleaner combustion with minimal harmful emissions. Glycine ($C_2H_5NO_2$) served as the fuel, while the corresponding metal nitrates functioned as oxidizing agents. The synthesis was carried out using an optimized oxidizer-to-fuel ratio of 70:30 by weight to ensure efficient combustion and controlled nanoparticle formation.

2.1 Synthesis of NiO and FeO Nanopowders

Nickel(II) oxide (NiO) and iron(II) oxide (FeO) nanopowders were synthesized using a solution combustion route, following a similar protocol for both materials. Precisely weighed quantities of the respective metal nitrate precursors nickel(II) nitrate hexahydrate ($Ni(NO_3)_2{\cdot}6H_2O$) for NiO and ferric nitrate ($Fe(NO_3)_3{\cdot}9H_2O$) for FeO were dissolved in distilled water along with glycine, which served as the combustion fuel. Each mixture was magnetically stirred for approximately 30 minutes to ensure thorough homogenization at the molecular level.

The clear precursor solutions were subsequently heated on a combustion mantle or hot plate. As the temperature increased, gradual evaporation of the solvent resulted in the formation of a viscous gel. Upon reaching the critical ignition temperature, typically above 200 °C, the gels underwent rapid and self-propagating combustion. This highly exothermic process proceeded without further external energy input, producing lightweight, porous, foam-like ashes corresponding to the final NiO and FeO nanopowders.

The combustion synthesis method facilitated efficient conversion of the precursor materials into nanoscale oxide products while enabling controlled morphology and high porosity attributes beneficial for subsequent photocatalytic applications.

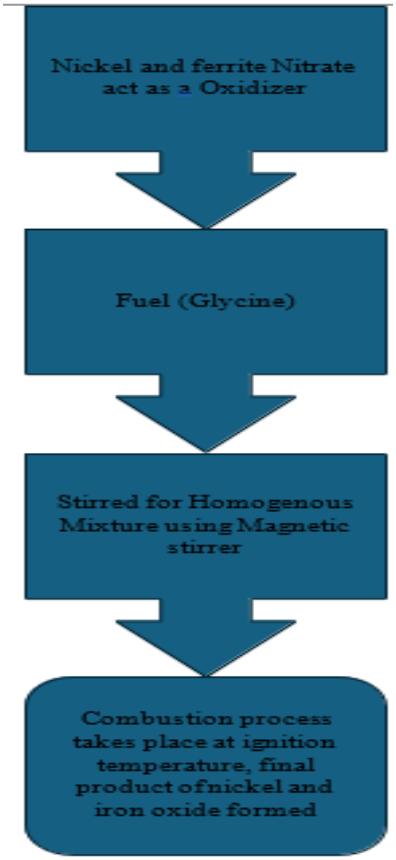

Figure 1 Systematic representation of combustion technique

Results and Discussion

3.1 X-ray Diffraction Analysis

X-ray diffraction (XRD) was employed to investigate the crystalline structure and phase purity of the synthesized NiO and FeO nanopowders. Figure 2 illustrates the diffraction profiles recorded for both samples using CuKα radiation with a characteristic wavelength of 1.5406 Å. The diffraction patterns exhibit well-defined peaks, confirming the crystalline nature of the metal oxides.

All observed reflections for NiO and FeO correspond precisely to the standard data reported in the Joint Committee on Powder Diffraction Standards (JCPDS) file No. 89-1397. The absence of additional or spurious peaks in the diffractograms indicates that both nanopowders are single phase materials with no detectable secondary impurities. This confirms the effectiveness of the combustion synthesis route in yielding phase-pure oxide nanoparticles.

The average crystallite size (D) for both samples was estimated using the Debye–Scherrer equation:

$$D = \frac{0.94\lambda}{\beta\cos\theta} \quad (1)$$

where

- D is the crystallite size,
- λ is the wavelength of CuKα radiation,
- β is the full width at half maximum (FWHM) of the selected diffraction peak, and
- θ is the Bragg diffraction angle.

The FWHM values required for these calculations were extracted using Origin software. According to the equation, the crystallite size is inversely related to the peak broadening: a larger β corresponds to smaller grain dimensions. This relationship confirms that the broadened diffraction peaks observed in the pattern are characteristic of nanoscale crystallites.

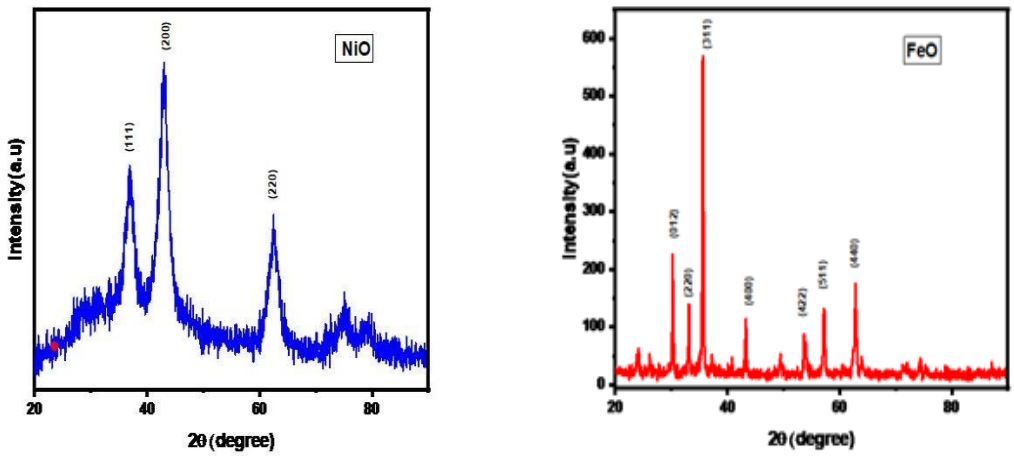

Figure 2 XRD pattern for FeO and NiO

The JCPDS reference patterns represent diffraction data for bulk crystalline materials; therefore, the corresponding peaks exhibit extremely narrow widths, with full width at half maximum (FWHM) values that are nearly zero. In contrast, nanoscale materials display noticeable peak broadening. As particle size decreases, the FWHM increases, reflecting the well-known inverse relationship between crystallite size and peak width. A summary of the calculated XRD parameters for NiO and FeO is presented in Table 1.

The interplanar spacing (d) for each diffraction peak was determined using Bragg's law:

$$2d\sin\theta = \lambda \quad (2)$$

where d denotes the spacing between lattice planes and λ is the wavelength of CuKα radiation. The calculated d-values for all peaks confirm the expected crystal structure for both samples.

Sample	Crystalline size D (mm)	Lattice parameter a (Å)
FeO	13.65	8.4590
NiO	12.34	8.3670

Table 1 XRD analysis for FeO and NiO

The NiO sample exhibits its most intense diffraction peak at 36.27°, while the FeO sample shows a corresponding maximum at 36.38°, both of which are attributed to the (311) and (200) crystallographic planes. Average crystallite sizes, calculated by considering all major diffraction peaks, were found to be 12.34 nm for NiO and 13.65 nm for FeO. Alternatively, crystallite size may also be computed solely from the highest-intensity peaks [(311) and (200)], which typically provide the most reliable estimates.

The slightly larger crystallite size observed for FeO can be attributed to the greater ionic radius of Fe^{3+} compared to Ni^{2+}, which influences lattice expansion during nanoparticle formation. The XRD results further indicate that Ni^{2+} and Fe^{3+} ions occupy their respective interstitial lattice positions within the NiO and FeO crystal structures.

3.2 High-Resolution Transmission Electron Microscopy (HRTEM)

High-Resolution Transmission Electron Microscopy (HRTEM) was employed to examine the morphology and particle size characteristics of the synthesized NiO and FeO nanoparticles. The micrographs indicate that the particles tend to form agglomerated clusters, which is a common feature in nanoscale oxide materials due to their high surface energy. At higher magnification (2 nm scale), well-defined lattice fringes are visible, confirming the crystalline nature of the samples.

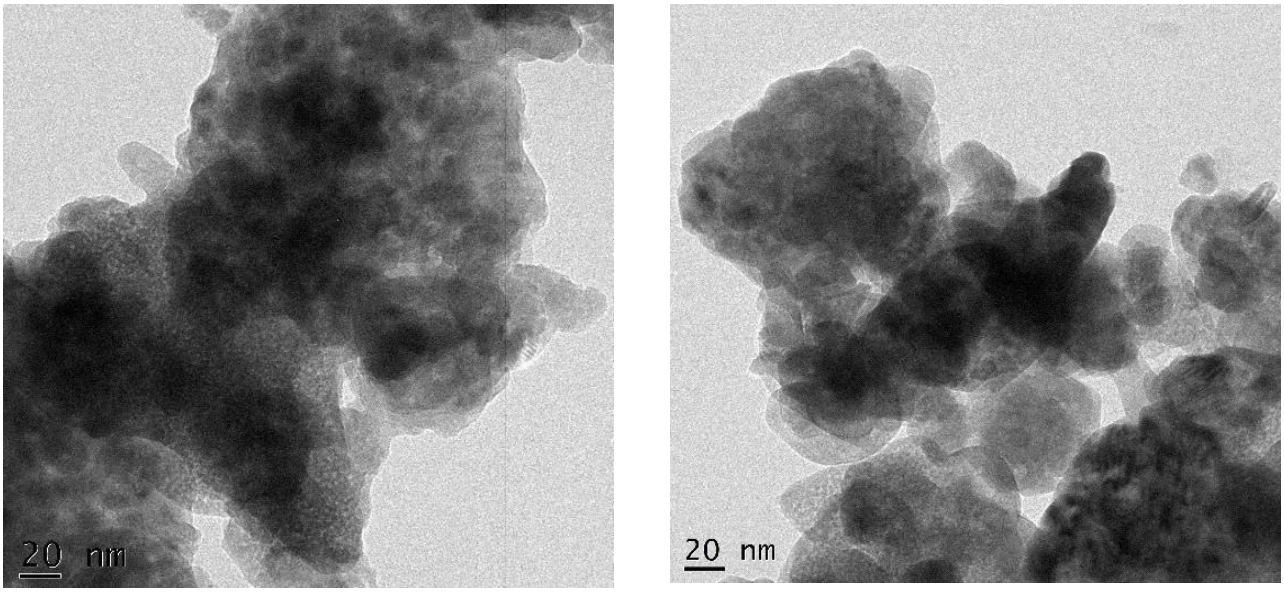

Figure 3, HRTEM image of (i) NiO (ii) FeO

3.3 Uv–Visible Spectroscopy Analysis

The incorporation of metal ions within the synthesized NiO and FeO nanoparticles was further investigated using Uv-Visible spectroscopy at room temperature. The absorption spectra for both oxide nanomaterials are presented in Figure 4. Analysis of these spectra enabled the estimation of the optical band gap energies, which were determined using the Kubelka–Munk (K–M) function derived from the measured absorbance data. This approach provides a reliable evaluation of the electronic transitions and confirms the semiconductor behavior of the synthesized nanoparticles.

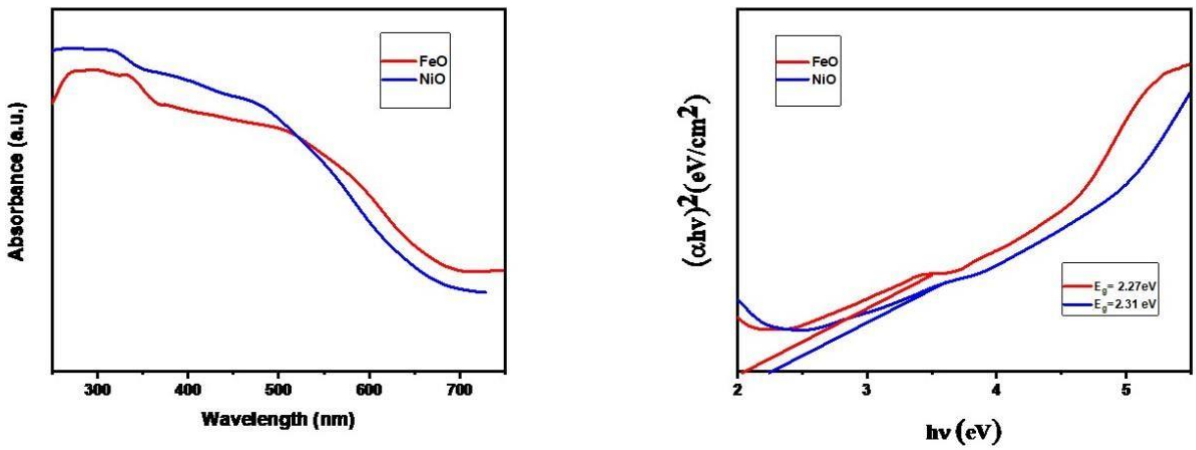

Figure 4 Uv- Visible spectra of NiO and FeO

The optical band gap of the synthesized nanoparticles was estimated using the Tauc relation:

$\alpha h\nu = (h\nu - E_g)^{1/n}$

In this expression, α is the absorption coefficient, $h\nu$ is the photon energy, A is a proportionality constant, and E_g denotes the optical band gap. For materials exhibiting direct electronic transitions, the exponent n assumes a value of 1/2. The band gap is obtained by plotting $(\alpha h\nu)^2$versus $h\nu$ (Kubelka–Munk representation) and extrapolating the linear portion of the curve to intersect the energy axis, where the intercept corresponds to E_g.

Using this method, the NiO sample was found to possess an optical band gap of approximately 2.3 eV. Both NiO and FeO exhibited lower band gap energies than their respective bulk counterparts, indicating a noticeable red shift. For FeO, the reduction in band gap is primarily associated with the strong *sp–d* exchange interactions between the conduction-band electrons and the localized *d*electrons of Fe^{2+} ions, which leads to band structure modification and enhanced absorption in the lower-energy (visible) region.

3.4 Fourier Transform Infrared (FTIR) Spectroscopy

Nanomaterials typically exhibit a higher surface-to-volume ratio compared to their bulk counterparts, which accentuates their unique surface chemical properties. Fourier Transform Infrared (FTIR) spectroscopy was employed to investigate the vibrational characteristics of the synthesized NiO and FeO nanoparticles, with the resulting spectra presented in Figure 5. Understanding the vibrational signatures of these oxides is essential for confirming their chemical composition and distinguishing between the two materials.

FTIR measurements were conducted over the range of 400–4000 cm^{-1} to capture all relevant vibrational modes. Broad bands observed near 3400 cm^{-1} and 1600 cm^{-1} are attributed to O–H stretching and bending vibrations, respectively, indicating the presence of residual water from the synthesis process.

In the NiO spectrum, characteristic absorption bands were observed at 822 cm^{-1}, 636 cm^{-1}, and 492 cm^{-1}, which are associated with the vibrational modes of Ni–O bonds, confirming the formation of the wurtzite crystalline phase. In contrast, the FeO nanoparticles displayed distinct bands at 1476 cm^{-1}, 662 cm^{-1}, and 478 cm^{-1}, corresponding to vibrational modes arising from the octahedral and tetrahedral coordination environments of Fe^{2+} ions. These observations validate the successful synthesis of both NiO and FeO and provide insights into their local structural arrangements.

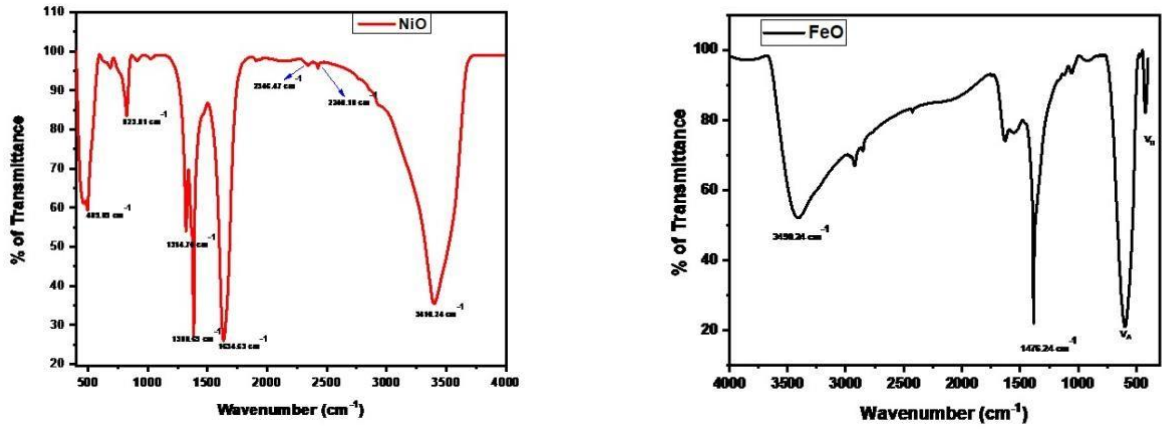

Figure 5 FTIR analysis of NiO and FeO

3.5 Fourier Transform Raman Spectroscopy

Raman scattering arises from the inelastic interaction between incident photons and phonons, the quantized vibrational modes of a crystal lattice. This process primarily occurs when photons interact with electrons, which act as intermediaries. The interaction is intrinsically weak, and ultraviolet (UV) phonons typically do not contribute directly. Instead, incident photons excite electrons into a transient "virtual state," creating electron–hole pairs. These pairs subsequently scatter by absorbing or emitting phonons before recombining and emitting photons, restoring the material to its original electronic state. The analysis of the scattered photons provides detailed insights into both the vibrational and electronic characteristics of the material.

Both NiO and FeO nanoparticles crystallize in a hexagonal wurtzite structure, exhibiting C_{6v} symmetry. Group theory predicts that the zone-center optical phonon modes for such structures are classified as $A_1 + 2B_1 + E_1 + 2E_2$. Among these, both Ni and Fe contribute to modes that are active in Raman and infrared (IR) spectroscopy. The polar modes, such as A_1 and E_1, are further divided into longitudinal optical (LO) and transverse optical (TO) components. The E_2 mode is non-polar and Raman-active but IR-inactive, whereas the B_1 mode is silent, remaining inactive in both Raman and IR measurements.

The Raman spectra obtained for NiO and FeO, illustrated in the accompanying figure, exhibit peaks consistent with the predicted phonon modes, thereby confirming the crystalline structure and providing further evidence of the material's vibrational properties.

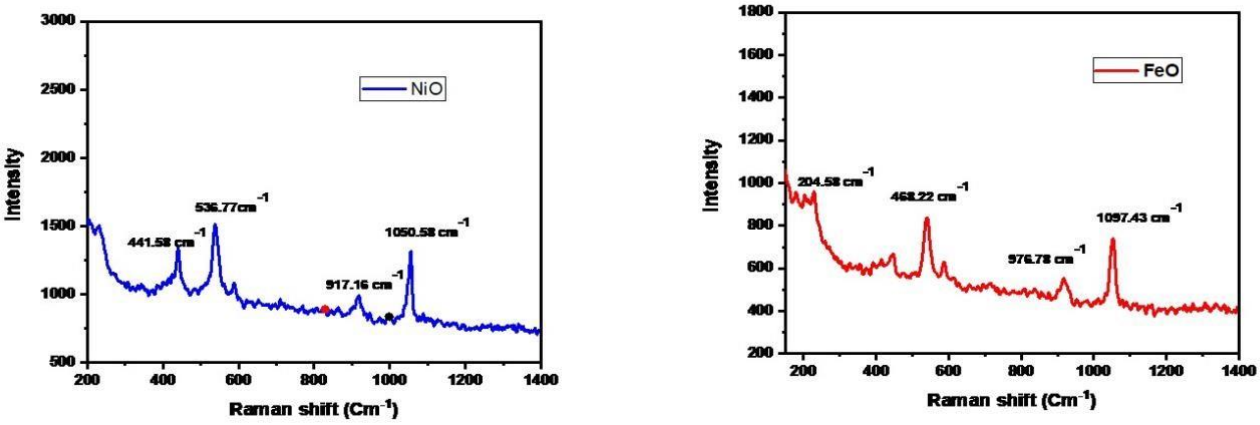

Figure 6 FT RAMAN analysis of NiO and FeO

The frequency at 204 cm^{-1} is assigned to the E_2(low) mode, which signifies the non-polar vibration of the heavier Ni and Fe molecules oscillating within their sub-lattice structure. The peak at 441 cm^{-1} corresponds to the E_2(high) mode, which represents the shifting or displacement of oxygen atoms from their lattice positions. A peak detected at 917 cm^{-1} indicates a functional group inherent to the glass material used for mounting the samples during the FT Raman analysis; specifically, it represents the asymmetric stretching of the Si-O bond within the substrate. Finally, the peak observed at 1050.28 cm^{-1} is frequently claimed by numerous papers in the field to be a result of multi-phonon scattering events.

3.6 SEM Analysis

Surface morphology characterization of the synthesized nanoparticles revealed densely packed, well-oxidized agglomerates consistent with iron oxide and nickel oxide nanostructures. Elemental analysis confirmed the presence of Ni, Fe, and O, indicating the successful formation of phase-pure NiO and FeO nanoparticles without detectable impurities. The nanoparticles predominantly exhibited a spherical shape with uniform morphology. Additionally, a strong correlation was observed between the average particle size measured from electron microscopy images and the crystallite size calculated from Xray diffraction (XRD) data, corroborating the structural and morphological consistency of the synthesized material

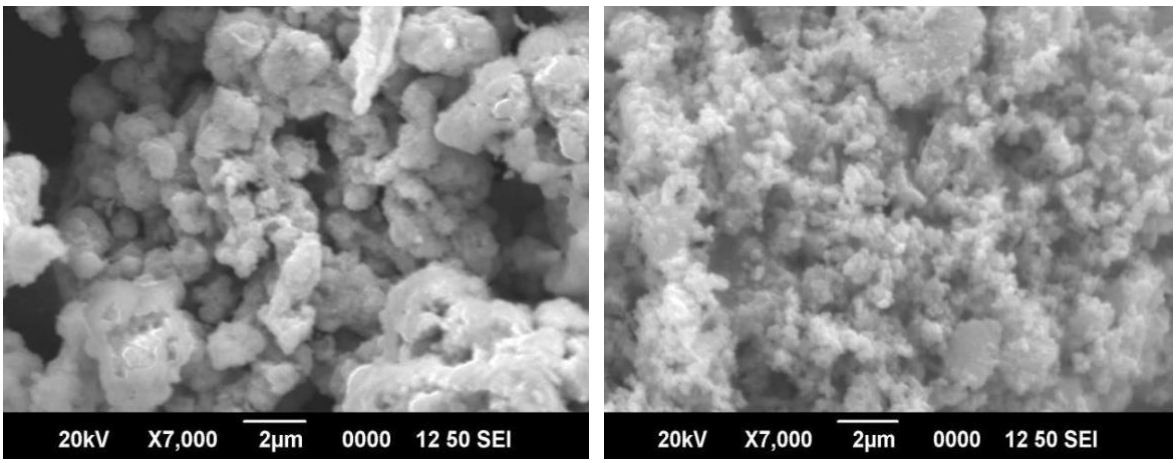

Figure 7. SEM image of NiO and FeO

3.7 Photocatalytic Activity

The photocatalytic performance of the synthesized NiO and FeO nanoparticles was evaluated through the degradation of an organic dye in aqueous solution under visible light irradiation. A 125 W mercury lamp served as the light source. In a typical experiment, 50 mg of the nanoparticle catalyst (NiO or FeO) was dispersed in 50 mL of a 10 mg/L Methylene Blue (MB) solution. Prior to illumination, the suspension was magnetically stirred in complete darkness for 30 minutes to establish adsorption–desorption equilibrium between the dye molecules and the catalyst surface.

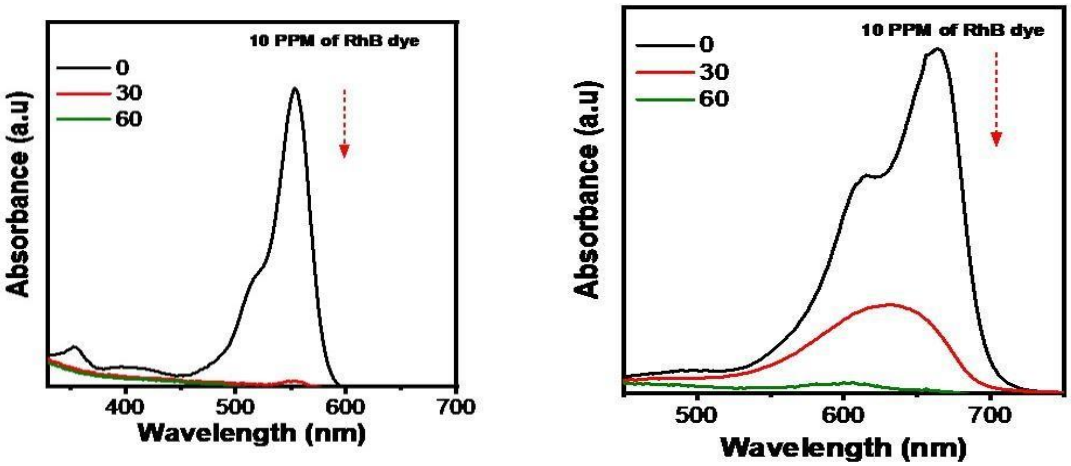

Figure 8. Change in spectra of Rhodamine B with time in the presence of NiO and FeO Nanoparticles.

After equilibration, 2 mL of 30% H_2O_2 was added to the system to enhance the generation of reactive oxygen species, and the mixture was irradiated with visible light. Aliquots of 3 mL were withdrawn at predetermined time intervals and immediately centrifuged to separate the nanoparticles. The concentration of the residual MB in the supernatant was measured using a UV–Visible spectrophotometer to monitor the degradation process.

The results demonstrated that both NiO and FeO nanoparticles exhibited photocatalytic activity; however, NiO showed superior performance in degrading the dye compared to FeO. This enhanced efficiency is attributed to the optimized electronic structure and favorable charge carrier dynamics of NiO, which promote effective generation and separation of photogenerated electron–hole pairs under visible light irradiation.

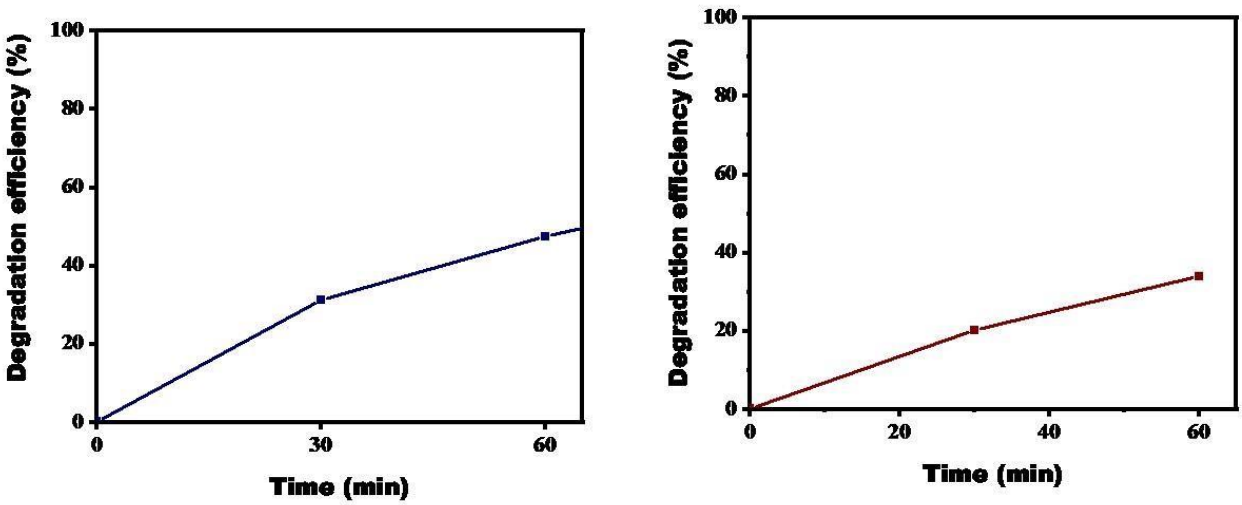

Figure 9. Effect of NiO and FeO on degradation Efficiency

sample	Degradation (%)	Rate constant
NiO	59.2	0.006
FeO	39.9	0.012

Table 2 Effect of NiO and FeO on degradation efficiency

Conclusion

NiO and FeO nanoparticles were successfully synthesized via a rapid, cost-effective solution combustion method, producing phase-pure, crystalline materials with nanoscale dimensions.

Structural characterization (XRD, TEM/SEM) confirmed well-defined crystallinity and predominantly spherical morphology, while elemental analysis verified their purity. Optical studies revealed reduced band gap energies compared to bulk materials, and

FTIR and Raman analyses confirmed the retention of wurtzite symmetry and characteristic vibrational modes. Photocatalytic experiments demonstrated effective degradation of organic dyes under visible light, with NiO showing superior activity due to favorable charge carrier dynamics. These findings highlight the potential of NiO and FeO nanoparticles for environmental remediation and other photocatalytic applications.

Acknowledgment

The authors express their sincere gratitude to the Management and the Principal of Auxilium College (Autonomous), Vellore, for providing the necessary infrastructure and research facilities to carry out this work. We are thankful to the Head of the PG & Research Department of Physics for constant encouragement and academic support.

We also extend our heartfelt thanks to all faculty members and laboratory staff for their valuable guidance, technical assistance, and cooperation during the course of this research. Finally, we acknowledge our family members and friends for their continuous motivation and moral support.

Financial support and sponsorship

Nil.

Conflicts of interest

The authors declare that there are no conflicts of interest regarding the publication of this paper.

Reference

1. M. A. Amin, "Water pollution: Causes, effects, and solutions," *Water Sci. Technol.*, vol. 79, no. 10, pp. 1958–1975, 2019.
2. L. Li, et al., "Advances in conventional water treatment methods," *J. Water Process Eng.*, vol. 35, 101185, 2020.
3. J. Smith, "Limitations of traditional purification techniques for persistent organic pollutants," *Environ. Res.*, vol. 188, 109841, 2021.
4. S. R. Bakardjieva, "Photocatalysis: A sustainable solution for environmental remediation," *Catal. Today*, vol. 347, pp. 1–13, 2020.
5. P. K. Jha, "Mechanism of pollutant degradation using light-driven processes," *ACS Appl. Mater. Interfaces*, vol. 12, no. 45, pp. 50050–50065, 2020.
6. H. J. Seo, "Stability and affordability of semiconductor oxides in catalysis," *Mater. Sci. Semicond. Process.*, vol. 105, 104768, 2020.
7. Y. Su, "A review on TiO2 based photocatalysts," *J. Am. Ceram. Soc.*, vol. 104, no. 5, pp. 2487–2512, 2021.
8. G. Liu, "Addressing wide band gap limitations in photocatalytic materials," *Chem. Rev.*, vol. 120, no. 16, pp. 8395–8421, 2020.
9. D. C. Sayle, "High rates of electron-hole recombination in benchmark photocatalysts," *J. Phys. Chem. Lett.*, vol. 11, no. 20, pp. 8920–8927, 2020.
10. A. K. Mishra, "Strategies for enhancing visible-light absorption and charge separation efficiency," *Appl. Catal. B Environ.*, vol. 280, 119420, 2021.
11. M. K. Ghosh, "Complex metal oxides: Tunable compositions for next-generation catalysis," *Dalton Trans.*, vol. 49, no. 30, pp. 10444–10461, 2020.
12. R. E. Schaak, "Rational design of perovskite and spinel materials for energy applications," *Acc. Chem. Res.*, vol. 54, no. 2, pp. 384–395, 2021.
13. S. F. Chin, "Surface engineering for enhanced pollutant interaction in catalysis," *ACS Omega*, vol. 5, no. 35, pp. 22288–22296, 2020.
14. Shah, M. A., & Ahmad, T. (2010). Principles of nanoscience and nanotechnology. Alpha Science International.
15. Chauhan, J., Shrivastav, N., Dugaya, A., & Pandey, D. (2017). Synthesis and characterization of Ni and Cu doped ZnO. Journal Nano medicine Nanotechnology, 8,1-8.
16. Jayalakshmi, M., Palaniappa, M., & Balasubramanian, K. (2008). Single step solution combustion synthesis of ZnO/carbon composite and its electrochemical characterization for supercapacitor application. Int. J. Electrochemist. Sci, 3, 96-103.
17. Under, P. G., Birajdar, S. D., Kathare, R. V., & Jadhav, K. M. (2018). Enhancement of Electrical Resistivity in Nickel Doped ZnO Nanoparticles. Procedia Manufacturing, 20, 477480.
18. Kumar, S. S., Venkateswarlu, P., Rao, V. R., & Rao, G. N. (2013). Synthesis, characterization and optical properties of zinc oxide nanoparticles. International Nano Letters, 3(1), 30.
19. Xiong, G., Pal, U., Serrano, J. G., Ucer, K. B., & Williams, R. T. (2006). Photoluminesence and FTIR study of ZnO nanoparticles: the impurity and defect perspective. physica status solidi c, 3(10), 3577-3581.
20. Vijayaprasath, G., Murugan, R., Mahalingam, T., & Ravi, G. (2015). Comparative study of structural and magnetic properties of transition metal (Co, Ni) doped ZnO nanoparticles. Journal of Materials Science: Materials in Electronics, 26(9), 7205-7213.
21. Ye, Z.; Kong, L.; Chen, F.; Chen, Z.; Lin, Y.; Liu, C. AComparative Study of Photocatalytic Activity of ZnS Photocatalyst's for Degradation of Various Dyes. Optik (Stuttg). 2018, 164, 345−354.
22. Hannachi, E.; Slimani, Y.; Nawaz, M.; Trabelsi, Z.; Yasin, G.; Bilal, M.; Almessiere, M.A.; Baykal, A.; Thakur, A.; Thakur, P.Synthesis, characterization, and evaluation of the photocatalytic properties of zinc oxide co-doped with lanthanides elements. J.Phys. Chem. Solids 2022, 170, 110910. [CrossRef]
23. Rizwan, K.; Bilal, M.; Slimani, Y.; Show, P.L.; Rtimi, S.; Roy, A.; Iqbal, H.M.N. Hydrogen-based sono-hybrid catalytic degradation and mitigation of industrially-originated dye-based pollutants. Int. J. Hydrogen Energy 2023, 48, 6597–6612. [CrossRef]

24. Lops, C.; Ancona, A.; Di Cesare, K.; Dumontel, B.; Garino, N.; Canavese, G.; Hérnandez, S.; Cauda, V. Sonophotocatalytic degradation mechanisms of Rhodamine B dye via radicals generation by micro- and nano-particles of ZnO. Appl. Catal. B Environ.2019, 243, 629–640. [CrossRef] [PubMed]
25. Sadiq, M.M.J.; Shenoy, U.S.; Bhat, D.K. NiWO4-ZnO-NRGO ternary nanocomposite as an efficient photo catalyst for degradation of methylene blue and reduction of 4 nitro phenol. J. Phys. Chem. Solids 2017, 109, 124–133. [CrossRef]
26. Da Silva, W.L.; Hamilton, J.W.J.; Sharma, P.K.; Dunlop, P.S.M.; Byrne, J.A.; Dos Santos, J.H.Z. Agro and industrial residues: Potential raw materials for photo catalyst development. J. Photochem. Photobiol. A 2021, 411, 113184. [CrossRef]
27. Muraro, P.C.L.; Wouters, R.D.; Pavoski, G.; Espinosa, D.C.R.; Ruiz, Y.P.M.; Galembeck, A.; Rech, V.C.; da Silva, W.L. Ag/TiNPS Nano catalyst: Biosynthesis, characterization and photocatalytic activity. J. Photochem. Photobiol. A 2023, 439, 114598. [CrossRef]
28. Kumar N.; Gusain, R.; Pandey, S.; Ray, S. S. Hydrogel Nano composite Adsorbents and Photocatalysts for Sustainable WaterPurification. Adv. Mater. Interfaces 2023, 10, 2201375.
29. Pandey, S.; Son, N.; Kang, M. Synergistic Sorption Performance of Karaya Gum Crosslink Poly(Acrylamide-Co-Acrylonitrile) @ Metal Nanoparticle for Organic Pollutants. Int. J. Biol. Macromol. 2022, 210 (April), 300−314.
30. Ellery, A. S.; Salem, S. S.; Elzaref, A. S.; Owda, M. E.; Eladawy,H. A.; Saeed, A. M.; Award, M. A.; Abou-Zeid, R. E.; Fouda, A.Multifunctional Cellulose Nanocrystal /Metal Oxide Hybrid, PhotoDegradation, Antibacterial and Larvicidal Activities. Carbohydr. Polym. 2020, 230, 115711.